

SAND EROSION MODELING IN GENERIC COMPRESSOR RIG TESTING

Lei-Yong Jiang¹, Xijia Wu¹ & Qi Yang¹

¹Aerospace Research Center, National Research Council of Canada
Contact author: Lei-Yong Jiang; email: lei-yong.jiang@nrc-cnrc.gc.ca

Abstract

Based on erosion coupon tests, a sand erosion model for 17-4PH steel was developed. The developed erosion model was validated against the results of compressor erosion tests from a generic rig and from other researchers. A high-fidelity computational fluid dynamics (CFD) model of the test rig was built, a user defined function was developed to implement the erosion model into the ANSYS CFD software, and the turbulent, two-phase flow-field in multiple reference frames was solved. The simulation results are consistent with the test results from the compressor rig and experimental findings from other researchers. Specifically, the sand erosion blunts the leading edge, sharpens the trailing edge, and increases pressure-surface roughness. The comparisons between the experimental observations and numerical results as well as a quantitative comparison with three other sand erosion models indicate that the developed sand erosion model is adequate for erosion prediction of engine components made of 17-4PH steel.

Keywords: compressor rig; erosion modeling; sand; 17-4PH steel

1. Introduction

Sand erosion has long been recognized as a component degradation factor of air-breathing engines. Due to the higher hardness of the sand compared to steel or titanium compressor blades, as well as the high velocities at the engine inlet, ingestion of sand or other particles can cause significant component erosion, which affects the performance of the propulsion system, and increases the cost of ownership, particularly for helicopters.

Sand erosion damage is dependent on many factors such as the blade geometry, operating condition, material/sand properties, and engine flow field. Both experimental and numerical studies have been carried out to determine the features and intensity of compressor and turbine blade erosion. Grant & Tabakoff [1] and Balan & Tabakoff [2] performed experimental erosion studies on single-stage axial compressor, made of 6061 aluminum alloy. The experimental results revealed blunted leading edges, sharpened trailing edges, reduced blade chords, and increased roughness of blade pressure-surfaces. Sugano et al. [3] reported similar findings regarding the changes produced by erosion in axial-induced draft fans of coal-fired boilers. They also found that blade-chord reduction and material removal from the pressure surface increased with particle size. Richardson et al. [4] carried out a diagnostic study on the JT9D high-pressure compressor and found that in general the changes correlated well with engine cycles, not with hours of engine service. Rotor-blade erosion was observed mainly in the outer 50% of the span, where significant reductions in the blade chord and thickness and changes in the leading- and trailing-edge geometries were observed. Hamed et al. [5] thoroughly reviewed erosion research in turbomachines and the associated degradation in engine performance caused by environment particle ingestion, and confirmed the above findings.

Recently, a compressor blade erosion test rig was designed, constructed and commissioned at the Royal Military College of Canada (RMC) [Leithead, 2013; Massouh, 2012]. Erosion tests for bare and coated 17-4PH steel blades were carried out, and the blades were impacted by garnet sand for 5 hours. The experimental results provide useful information for understanding the blade erosion phenomenon and coating effectiveness, and validating erosion models and numerical simulations.

To develop a sand erosion model, erosion coupon tests were carried out on 17-4PH steel blades at particle impact angles from 30° to 90° and velocities of 84 and 150 m/s respectively. In the testing, Al₂O₃ powder with an average size of 105 μm was used as erosion media. The 17-4PH steel exhibited both cutting and deformation wear damage in comparable amounts, with erosion rates in the range of 800 – 1300 μg/g above an impact angle of 30°. Following the work from Bitter [6] and Neilson & Gilchrist [7], Wu & Yang [8] derived a sand erosion model for 17-4PH steel.

In this paper, the above developed erosion model for the 17-4PH steel is implemented into a CFD software solver and validated against the results of the compressor rig tests performed by RMC. In the following sections, the RMC compressor erosion rig test, the CFD simulation domain and mesh, the numerical methods and results are presented and discussed. Finally, a few key findings are highlighted.

2. RMC Compressor Erosion Rig and High-fidelity CFD Model

2.1 RMC Compressor Erosion Rig

A sketch of the RMC compressor erosion rig is shown in Fig. 1. The rig was designed to rotate 16 blade assemblies at speeds up to 12,000 rpm. The blade assemblies were inserted into a dynamically-balanced 20.32 cm diameter AISI 4340 steel rotor that was driven by an aircraft gas turbine compressor gearbox and a 20 HP electric motor. The erosive media, garnet, was injected via a sand hopper into the rig, and to improve air/garnet mixing, a venturi mixer with a throat diameter of 89.2 mm was inserted in the housing pipe. A centrifugal blower supplied the air flow to the rig. Rig operating conditions were monitored from an operator station. The parameters monitored included rotor vibrations, rotor rpm, air flowrate, sand flow supply, etc. A full description can be found in Refs. [9 – 10].

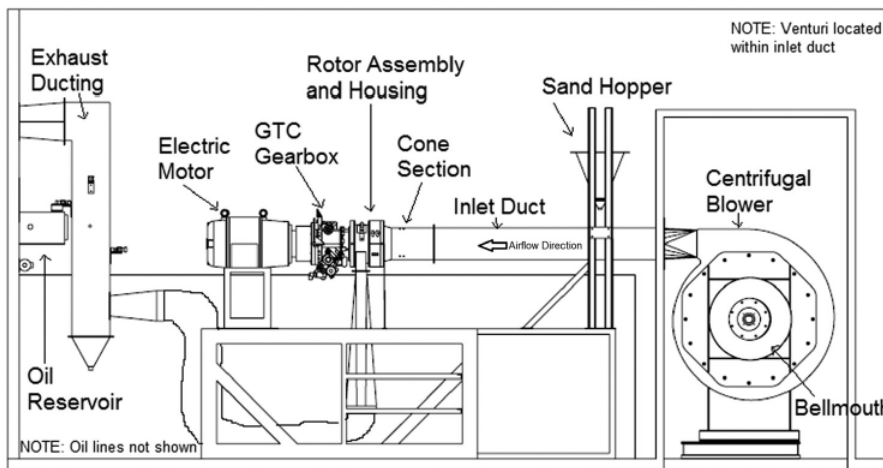


Fig. 1 Schematic of the RMC compressor erosion test rig [6]

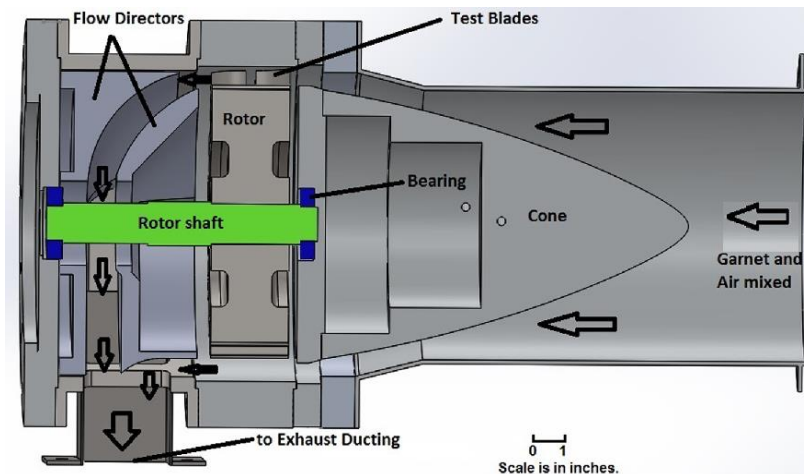


Fig. 2 Cross-section-view of the RMC compressor erosion rig test section [3]

Figure 2 is a cross-section view of the RMC compressor erosion rig test section, for clarity not all

blade assemblies are included. The mixture of air and garnet flows over the central cone and enters a 12.7 mm annulus flow passage. The cone length is 0.305 m [10 - 11]. Immediately downstream of the cone, the annulus passage becomes straight with a length of 8.1 mm to keep the flow perpendicular to the blade leading edge. Further downstream, there is a 6.6 mm gap between the cone section and rotor section, used to accommodate 16 balance adjustment screw-heads

2.2 Compressor Blade and Assembly

The test blade profile is named as V103, which is a modified version of a NACA 6505 airfoil. For the modified airfoil, the leading-edge radius is 0.19 mm, and the trailing edge radius is 0.15 mm. The modified blade profile normalized by the chord length is shown in Fig. 3. The test blade chord is 26.67 mm, and the span is equal to 12.7 mm minus the averaged tip clearance of 0.64 mm, i.e., 12.06 mm. The blade is made of 17-4PH steel, commonly used in turbine engines. More details are available in [6 - 7].

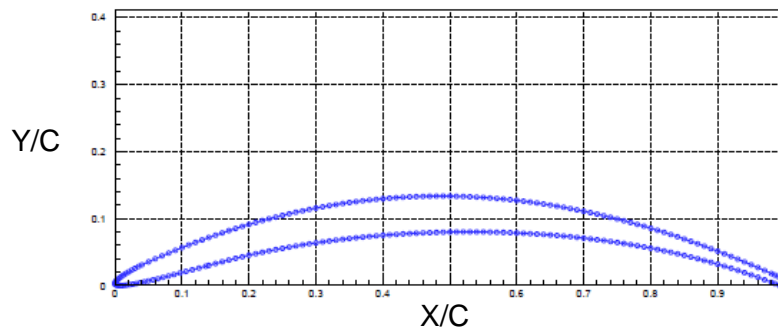


Fig. 3: The V103 blade profile

A top view of one blade-dovetail assembly is given in Fig. 4, where the test blade and dummy blade arrangement relative to the dovetail block is illustrated. To prevent a requirement for a larger electric motor, a two-blade arrangement was designed. The upstream blade acted as the compressor test article, and the downstream one simply flipped its pressure/suction sides and redirected the flow. In this way, the requirement for an excessively high-power input was avoided. The dimensions of the dovetails are: 25.4 mm wide and 58.4 mm long. The stagger angle is 27.7 degree, and the distance between two blades was 10.4 mm. Reference [6] contains additional details.

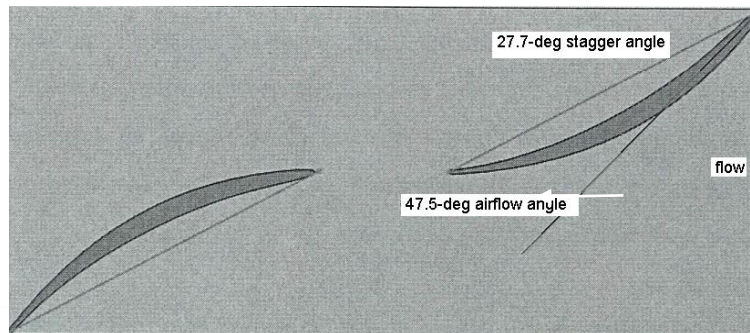


Fig. 4 Test blade and dummy blade arrangement of one blade-dovetail assembly

2.3 Computational Domain and Mesh

The computational domain and mesh are illustrated in Fig. 5, which is a 22.5° or $1/16$ sector of the flow field. The domain includes an 8-inch straight pipe segment, cone section, rotor section, and 6.6 mm slot. It consists of one blade assembly flow passage, begins downstream of the venturi diverging section, and is extended 20 mm downstream of the rotor section.

As observed in Fig. 5, fine grids were laid at the blade surfaces, in the downstream region of the cone section, as well as in the narrow tip clearance region. The tip clearance is only 0.64 mm, and 6 grids were generated in the vertical direction. The y^+ value is in a range of 20 - 55 for the blade, blade tip, and casing wall. Effort was made to keep y^+ values in the range of 30 - 150 for the remaining walls. A few meshes were created and preliminary runs were performed to improve the quality of numerical simulations. The solution mesh independence was checked, and the deviation between the 2.8 million and 6.9 million cell cases at the rotor middle cross-section was only 1.2% for the mean Mach number, and 0.69% for the maximum Mach number. Finally, a mesh of 4.3 million cells was used for all

simulations.

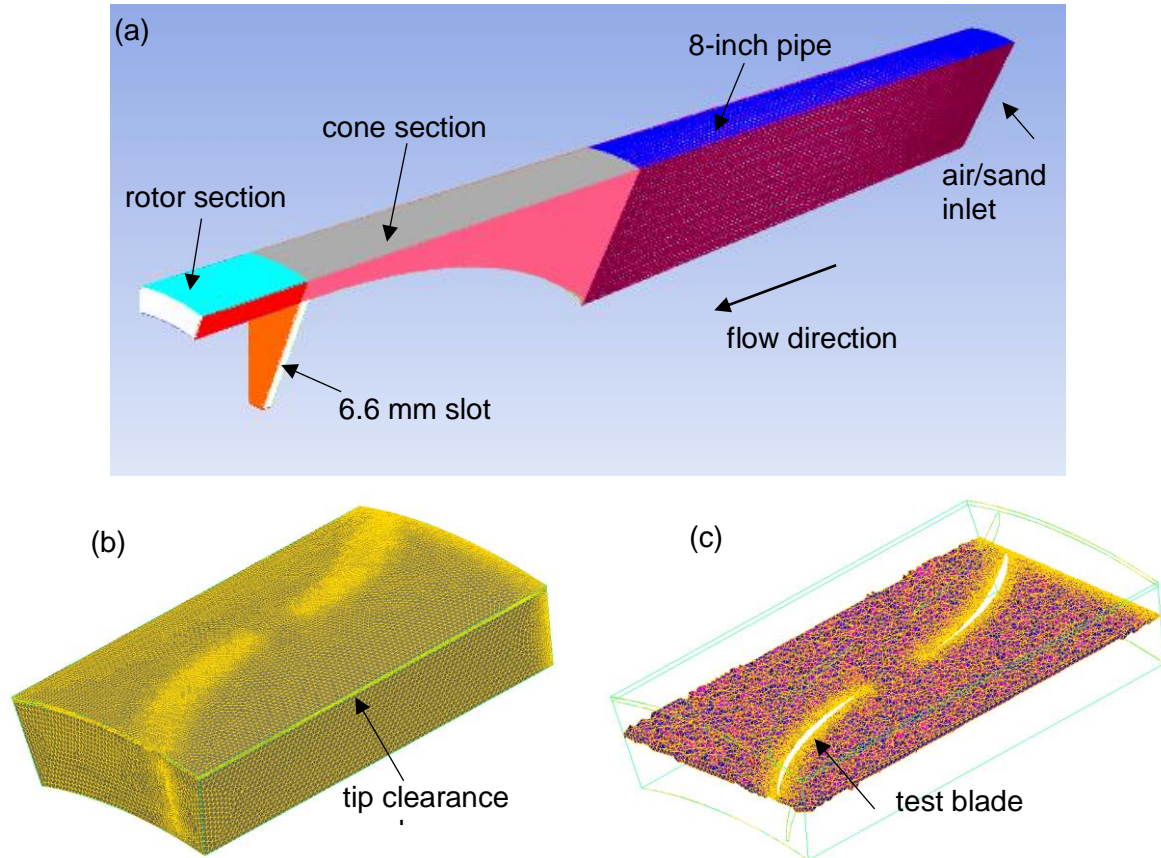


Fig. 5 Computational domain and mesh, (a) the whole domain and mesh, (b) the rotor section mesh, and (c) the mesh across rotor middle section

3. Numerical Methods

Two phase, compressible, turbulent flows in multiple reference frames were considered in the present work. A commercial software package, ANSYS CFD Premium, was used for all numerical simulations. To account for compressor blade erosion, the erosion model from Wu & Yang [8] was implemented into the software package. In the following sub-sections, the compressor input parameters, numerical approaches, implementation of the compressor erosion model, other physical models, and solution methods are briefly described.

3.1 Inputs Parameters of RMC Compressor Rig Testing

The input parameters from the RMC compressor test rig are given in Table 1. The air and sand inlet mass flowrates are 1/16 of the total air and sand flowrates in testing.

Table 1 Test rig operating conditions

| air mass flowrate m_{air} (g/s) | sand mass flowrate m_{sand} (g/s) | air/sand inlet T (K) | rotor (rpm) | rotor inlet Mach number |
|---|--|-------------------------|----------------|----------------------------|
| 69.4 | 0.148 | 300 | 10860 | 0.34 |

To account for the pressure loss behind the rotor section, the pressure at the computational domain exit was adjusted to match the Mach number of 0.34 at the rotor inlet. The pressure at the domain air inlet was defined as atmospheric, and the tiny pressure loss from the blower to the air inlet was neglected. For the 6.6 mm slot in Fig. 5(a), the cone section side was assigned as a stationary wall, and the rotor side was defined as a moving wall. Moreover, the rotor shaft ($d = 43$ mm) wall was also a moving wall.

Note that the corresponding sand concentration in air is 2.51 g/m^3 of air based on the air and sand flowrates in Table 1. This value is somewhat higher than the field measured values of 2.16 g/m^3 as the maximum, and 1.16 g/m^3 as an average [12]. In this sense, the RMC testing could be considered as an accelerated erosion case.

As mentioned earlier, garnet was used as the erosion media to represent sand in the rig testing, and Table 2 shows the particle distribution by size and weight.

Table 2 Particle distribution by size and weight for Barton UT220 garnet abrasive

| size (µm) | 106-125 | 90-105 | 75-89 | 63-74 | 53-62 | 45-52 | <45 |
|-------------|---------|--------|-------|-------|-------|-------|-----|
| % in weight | 5 | 21 | 28 | 22 | 15 | 5 | 4 |

The specific gravity of the garnet abrasive is 4000 kg/m³ and the Mohs hardness is 7.5-8.5 [13].

3.2 Simulations in Multiple Reference Frames and Eulerian-Lagrangian Approach

As the simulation concerns rotating machinery, the computational domain includes both stationary and moving components, i.e., the standing rig components and rotating rotor, respectively. A moving reference frame concept is introduced to render problems that are unsteady in the stationary frame steady with respect to the moving frame. The details of the steady Favre-averaged conservation equations in an inertial or stationary reference frame, and the flow velocity transformation between the stationary and moving frames can be readily found in [14 – 15].

In the present study, two reference frames, one stationary and one moving, are employed, and the mixing-plane approach is used for interfacing between these two frames. The main advantage behind the mixing-plane approach is that each fluid zone can be solved as a steady-state problem. The flow data at the mixing plane interface are averaged in the circumferential direction at the cone section outlet and rotor inlet boundaries. By performing circumferential averages along 66 radial stations in the mixing plane, the “profiles” of flow variables can be defined, and then used to update boundary conditions of the cone and rotor sections at the mixing plane. Despite the simplifications inherent in the mixing-plane approach, the resulting solutions can provide reasonable results of the time-averaged flow field [16]. Considering the speed of the blade rotation, 10,860 rpm, it is anticipated that the effect of the unsteadiness on the flow field would fade out.

The traditional Eulerian-Lagrangian approach is used to solve two-phase, turbulent, compressible flows in the two reference frames. For the present work, the volume fraction of garnet particles is negligibly small, 6.7E10⁻⁷, and thus the dilute discrete Lagrangian particle tracking method is an ideal approach without compromising the numerical solutions [17]. With this approach, the fluid phase is treated as a continuum by solving a set of governing equations, while the dispersed solid phase is solved by tracking a large number of particles through the calculated flow domain. The exchanges of momentum, mass, and energy between particles and fluid can be included if necessary.

The drag coefficients for both spherical and non-spherical particles are based on comprehensive experimental measurements [18 - 19]. For sand particles, a shape factor of 0.516 is suggested [20 - 21]. In the numerical simulations, for each group of particles in Table 2, the Rosin-Rammler size distribution was assumed and there were 2620 particle streams. As a result, there were a total of 18340 particle injection streams.

3.3 Particle Rebound Characteristics

It is recognized that particle rebound characteristics at walls play an important role in particle trajectory calculations. Considerable research in this area was conducted by Wakeman and co-workers [20, 22 & 23]. The experiments were carried out with 165 µm silica particles impinging on 2025 AL, INCO 718 and Ti 6-4 target walls with the impinging angles 15⁰ – 90⁰ and particle velocities 27 – 273 m/s. They pointed out that particle rebound characteristics were generally influenced by impingement angle, and not significantly affected by target material or temperature tested. The semi-empirical coefficients of restitution for tangential and normal velocities, COR_t and COR_n, before and after collision obtained from their measurements are used in the present work

$$COR_t = \frac{v_{t2}}{v_{t1}} = -3.562 \times 10^{-6} \alpha^3 + 6.427 \times 10^{-4} \alpha^2 - 2.897 \times 10^{-2} \alpha + 0.988 \quad (1)$$

$$COR_n = \frac{v_{n2}}{v_{n1}} = -2.605 \times 10^{-6} \alpha^3 + 4.752 \times 10^{-4} \alpha^2 - 3.072 \times 10^{-2} \alpha + 0.993 \quad (2)$$

where v_t and v_n are particle tangential and normal velocity components, α is particle impact angle in degrees, and the subscripts 1 & 2 indicate particle parameters before and after collision, respectively. The variations of tangential and normal coefficients of restitution with the particle impact angle are

illustrated in Fig. 6.

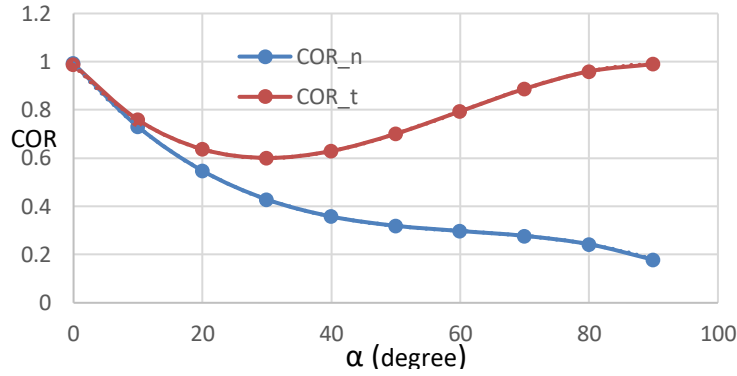


Fig. 6 Variation of COR_t and COR_n with particle impact angle

To model turbulent momentum transfer in the flow field, the SST k-ω model (the shear-stress transport-model) was applied. This model has illustrated major improvements in the prediction of adverse pressure gradients and separation flows over the standard k-ω and k-ε models, and has been widely used in turbine machinery flows [24]. The turbulence scalar transfers were calculated based on the modelled momentum transfer, where the turbulence Prandtl and Schmidt numbers of 0.75 were used. At the wall boundaries, the enhanced wall treatments were used for both turbulence kinetic energy and specific dissipation rate, where the viscous sublayer and the logarithmic layer formulations were smoothly blended [ANSYS Canada Ltd., 2018].

3.4 Erosion Model Implementation and Check

As mentioned, Wu & Yang [8] carried out erosion experimental studies on 17-4PH steel coupons and developed an erosion model for 17-4PH compressor blades. From these tests, the erosion rate (or ratio of the target mass loss to the mass of sand particles impinging on the target) for the 17-4PH steel can be evaluated by the following equations in unit of g/g:

$$\Delta W_a = \frac{1}{2} \Delta m_a U^2 \cos^2 \alpha \sin(n\alpha) / \varphi + \frac{1}{2} \Delta m_a (U \sin \alpha - K)^2 / \varepsilon \quad \alpha \leq \alpha_0 = \pi/2n \quad (3)$$

$$\Delta W_b = \frac{1}{2} \Delta m_b U^2 \cos^2 \alpha / \varphi + \frac{1}{2} \Delta m_b (U \sin \alpha - K)^2 / \varepsilon \quad \alpha \geq \alpha_0 = \pi/2n \quad (4)$$

where α is the impact angle, α₀ stands for the impact angle at which the horizontal velocity equals zero when the particle leaves the surface, Δm_a and Δm_b are the accumulated mass of particles impinging on the target material for the impact angle less and larger than α₀ respectively, U is the particle velocity magnitude, n and K are constants related to the target material, φ and ε represent the energies required to remove a unit mass from the target material through the cutting and deformation actions respectively. The model parameters are given in Table 3.

Table 3 Erosion model parameters

| material parameter | K (m/s) | n | φ [g (m/s) ²] | ε [g (m/s) ²] |
|--------------------|---------|---|---------------------------|---------------------------|
| value | 12.94 | 3 | 7.5E+06 | 1.2E+07 |

Considering local area and erosion duration, the local erosion rate can be defined as

$$LER = \Delta W / A * \dot{m} = (\Delta W_a + \Delta W_b) / A * \dot{m} \quad (5)$$

where A (mm²) is the local surface area, \dot{m} (g/hr) is the mass of sand particles impinging on the local area per unit time, and the unit LER is [g/(mm² hr)] which stands for the material mass loss per mm² per hour at the sand injection rate in the erosion testing, (0.1475g/s, the above sub-section 3.1).

Note that the erosion model input parameters include the four variable in Table 3, as well as the particle impact angle, mass, and velocity magnitude impinging on the metal wall. The last three parameters are obtained as particles travel through the flow field and impinge on the metal wall. The output parameters are local and total erosion rate (LER) or local and total mass loss at the defined test rig operating conditions.

A user-defined function is written to compile and link the above erosion model to the ANSYS CFD Premium flow solver. To ensure the erosion model was properly implemented, a few simple flows consisted of two pipes connected by a step with varying slope, as shown in Fig. 7, were used. For each numerical test case, the flow velocity was generated according to the erosion model test velocity, and one particle with a mass of one gram was released from a selected position in the flow. Trial and error were performed to match the experimental test conditions in terms of impact angle and velocity

magnitude. All the above seven model parameters and metal mass loss due to the particle impingement were printed, checked, and compared with the experimental data.

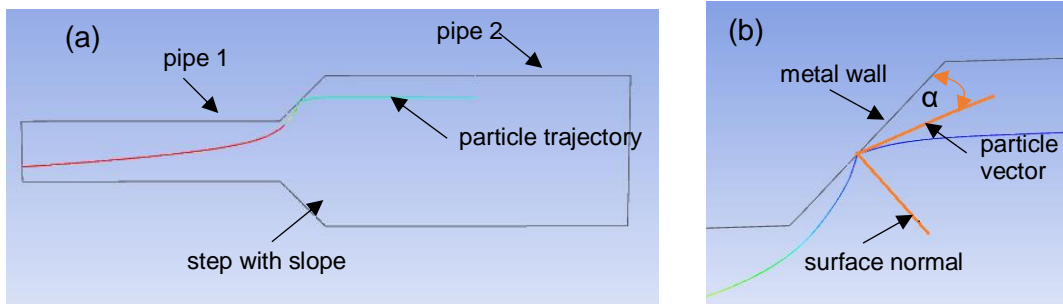


Fig. 7 A simple two-pipe flow to check erosion model implementation, (a) the flow field and a particle trajectory, and (b) the particle impact angle α

In Fig. 8, the erosion rates obtained from simulations with a particle flowrate of 1.0 g/s at a number of impact angles and velocities are compared with the model curves from Eqs. (3-4). It is clear that the computed results match the model curves, which indicates that the erosion model is correctly implemented into the flow solver.

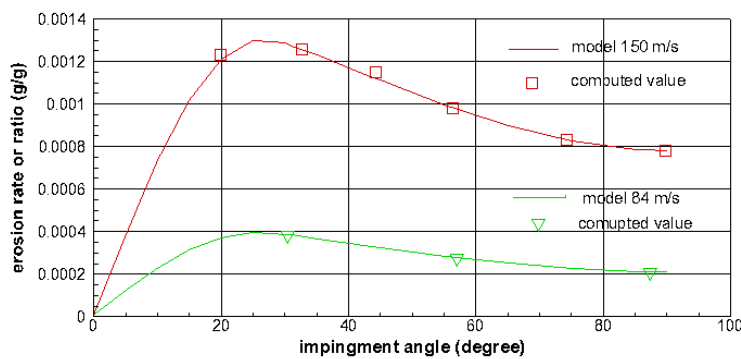


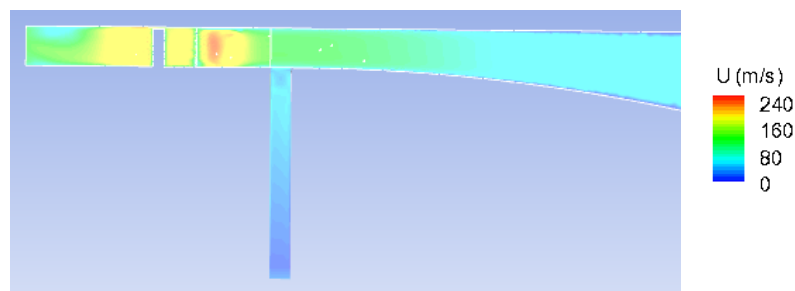
Fig. 8 Comparison between the computed and modeled erosion rates

A pressure-velocity coupled solver with a second-order accurate scheme was used to resolve the flow-field. As the flow reaches steady or quasi-steady, the scaled residuals of flow variables were less than 6×10^{-7} for velocity components and energy, and about 3×10^{-5} for turbulent variables. The monitored flow parameters remained unchanged at least for the first four significant digits. A LINUX cluster, 12-cores and 64 GB RAM was used for all simulations.

4. Results and Discussion

4.1 Flow-Field in the Rotor Vicinity

The distributions of velocity magnitude, Mach number and static pressure at the symmetric plane in the vicinity of the rotor section are displayed in Fig. 9. The flow velocity and Mach number increase gradually towards the rotor section and reach maxima in the rotor section due to the flow cross-section area gradual decrease. Consistent with the above, the static pressure gradually decreases towards the rotor section and reaches a minimum value in the rotor section.



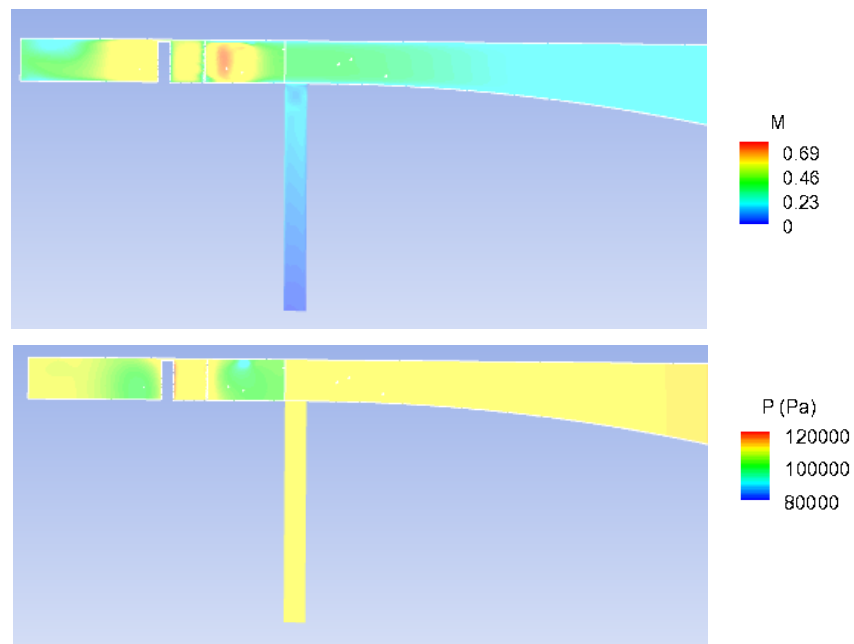
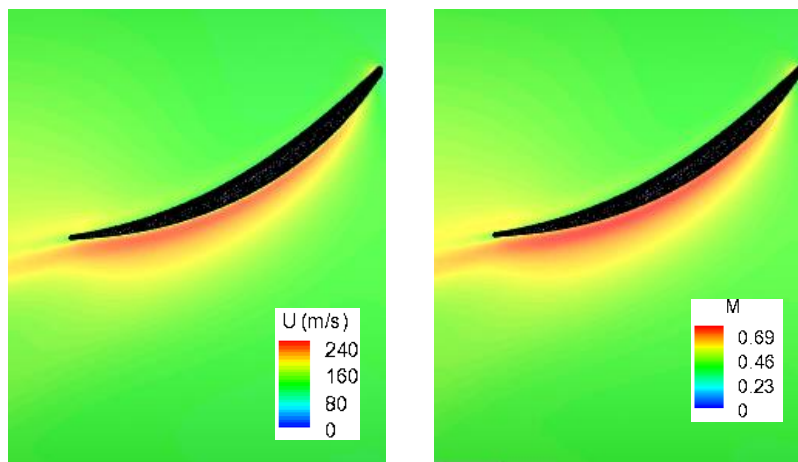


Fig. 9 Contours of velocity magnitude, Mach number and static pressure at the symmetric plane

The velocity, Mach number, static pressure, and velocity vector distributions across the mid-span of the test blade are illustrated in Fig. 10, viewed from top of the rotor section. The rotor rotates in the clockwise direction, looking upstream (or the blades are moving left to right). As expected, the velocity and Mach number contours are similar. The velocity and Mach number are low on the pressure side and gradually increase towards the trailing edge, and are high on the suction side, from $\sim 1/6$ downstream of the leading edge. The flow stagnation point is clearly indicated in the pressure plot, i.e., the highest pressure occurs at the blade leading edge. The pressure is low on most of the suction side due to flow acceleration, while along the pressure side the pressure gradually increases before decreasing near the trailing edge. In the vector plot, the velocity vectors stand for the combined incoming axial velocity and rotor rotating velocity, where the vector magnitude is coloured by Mach number.



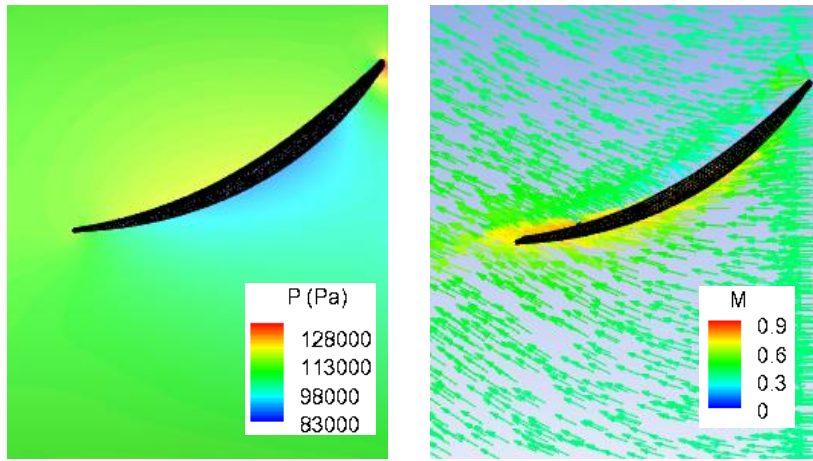


Fig. 10 Contours of velocity magnitude, Mach number and static pressure, as well as absolute vectors across the mid-span of the test blade

Figure 11 presents the distributions of velocity magnitude, Mach number and static pressure, and a velocity vector plot across the mid-tip-clearance over the test blade. In order to show the test blade tip location, these plots are rotated 180 degrees over the Z axis and viewed outwards from the rotor centre (put another way, the blades are moving right to left). The flow at this cross-section is complicated. It is affected by the stationary incoming flow from the cone, blade rotating flow, and stationary casing wall, as well as the associated interactions. As shown in the vector plot, the flow over the blade tip moves from the pressure side to the suction side, against the main flow direction, and the tip vortex is generated downstream of the suction side. Because of the tip leakage, a relative high velocity and Mach number region occurs at the front portion of the suction side, while the velocity and Mach number are relatively low over the pressure side. The pressure patterns are consistent with the velocity and Mach number distributions.

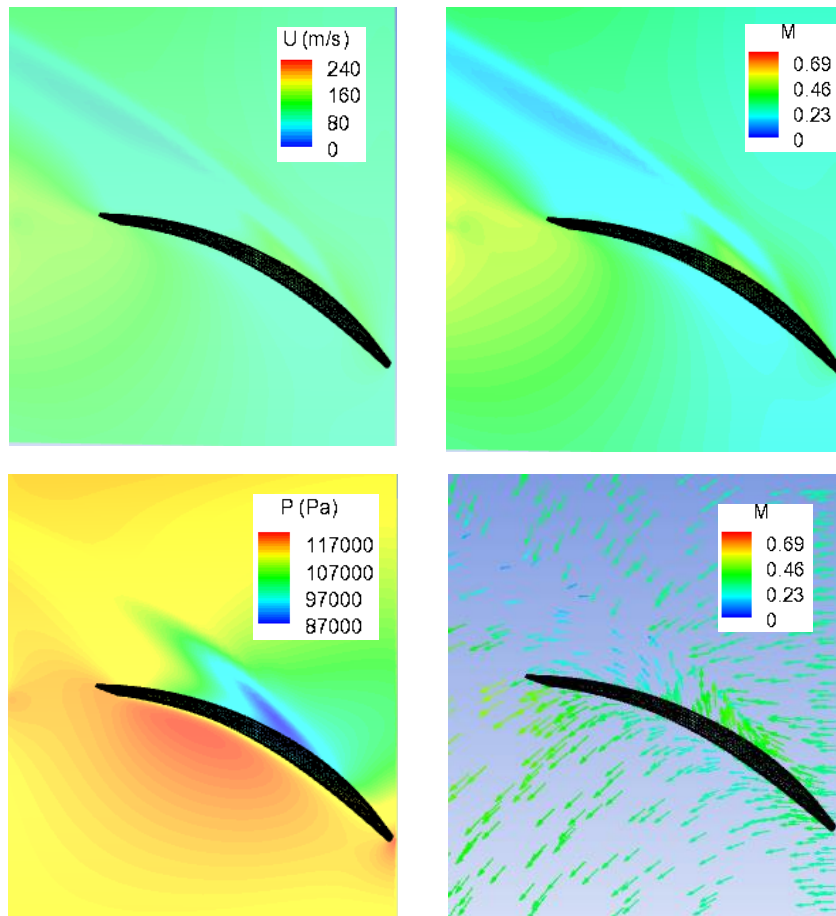


Fig. 11 Contours of velocity magnitude, Mach number and static pressure, as well as absolute vectors across the mid-tip-clearance over the test blade

The distributions of velocity magnitude, Mach number and static pressure at the mid-cross-section of

the 6.6 mm slot are illustrated in Fig. 12, where the 12.7 mm annulus inlet section is indicated by black lines. This more or less confined flow is influenced by the incoming annulus flow from the cone section, rotor rotating flow, stationary wall on the cone side, and moving walls on the rotor side and rotor shaft. In general, the slot flow is rotating around the rig longitudinal axis caused by the moving walls, and vortices occur just below the annulus channel generated by the incoming annulus flow. As seen in the three plots, the effect of the slot flow on the main annulus flow is negligible. The flow parameters gradually increase from the bottom to top, except that in the pressure plot there is a low-pressure region below the annulus flow. This low-pressure region is where a small vortex occurs across the 6.6 mm slot with its axis perpendicular to the flow longitudinal plane, and it is generated by the in-coming annulus flow. Detailed analysis is beyond the scope of the present work.

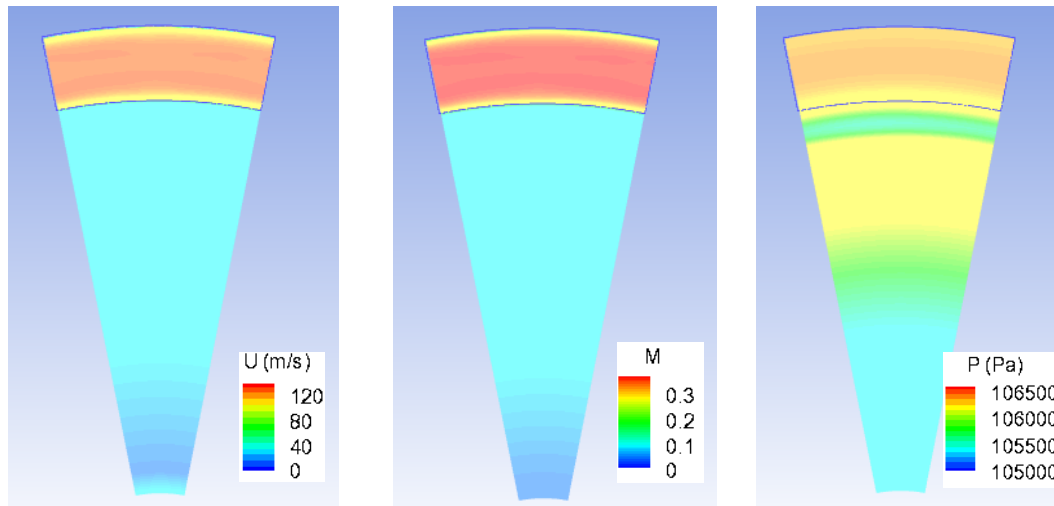


Fig. 12 Contours of velocity magnitude, Mach number and static pressure at the mid-cross-section of the slot

4.2 Particle Trajectories

Typical particle trajectories around the test blade are shown in Fig. 13 for particle diameters of 115, 68.5 and 22.5 μm , represented by red, green, and blue lines, respectively. Figure 14 gives representative flow path-lines passing through the test blade, where the flow path-lines follow the blade profile in general. In these two plots, the test blade and rotor periodic surfaces are shown in yellow color. The three path-lines across the blade indicate that the air flows over the blade tip through the tip clearance. The airflow at the rotor section entry experiences a sudden velocity increment, i.e., gaining a large rotating circumferential velocity; however, the particles cannot fully follow the airflow change due to their inertia. As seen in Fig. 13, for the particles starting at nearly the same upstream location, the larger the particle size, the further upstream the impingement point.

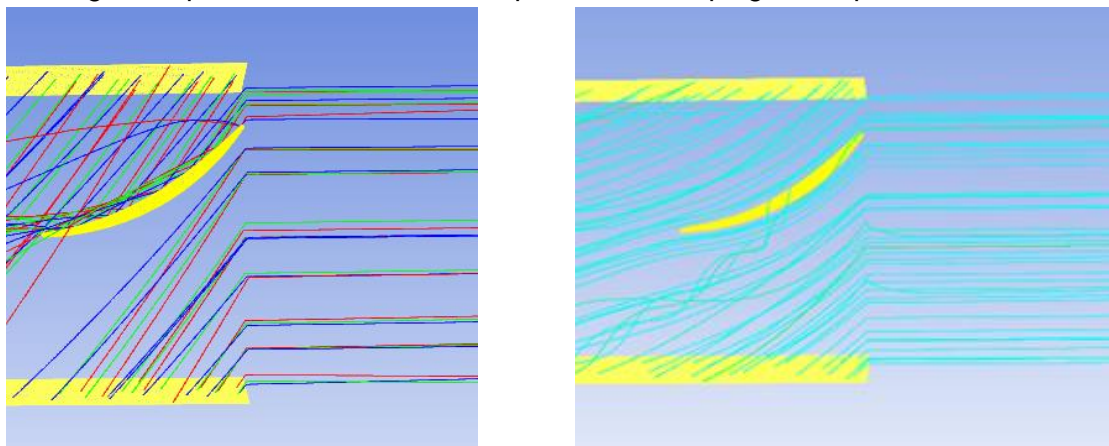


Fig. 13 Typical particle trajectories around the test blade for $d = 115, 68.5$ and $22.5 \mu\text{m}$, colored in red, green, and blue lines respectively

Fig. 14 Typical flow path-lines around the test blade

Figure 15 shows a number of particle trajectories traversing through the cone and rotor sections for $d = 115, 68.5$ and $22.5 \mu\text{m}$, respectively, where all walls are shown in yellow. Almost all particles impinge

on the test rig wall, bounce back and move forward in the flow passage. Their trajectories are different, depending on particle size, impact angle, and injection location at the air/sand inlet. Figure 16 displays some of sand particle trajectories passing through the rotor inlet cross-section for $d = 115, 68.5$ and $22.5 \mu\text{m}$. It is interesting to see that for this cone configuration, more particles enter the rotor section through the upper portion of the cross-section, and less particles enter the rotor section through the lower portion of the cross-section. This phenomenon is consistent with the observation by Richardson et al [4] on the JT9D high-pressure compressor, as mentioned earlier.

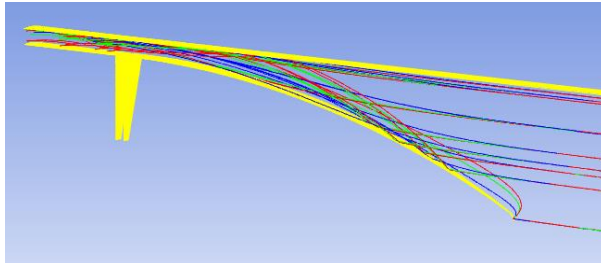


Fig. 15 Typical particle trajectories through the cone and rotor sections for $d = 115, 68.5$ and $22.5 \mu\text{m}$, colored in red, green, and blue lines

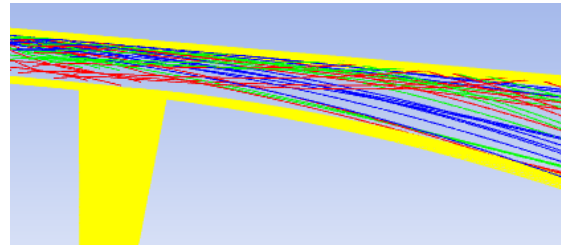


Fig. 16 Particle trajectories through the rotor inlet cross-section, $d = 115, 68.5$ and $22.5 \mu\text{m}$, colored in red, green, and blue

4.3 Sand Particle Accretion Rate, Velocity Magnitude and Impact Angle

The particle accretion rate is defined as the accumulated mass of sand particles impinging on the local metal surface per unit time, i.e.

$$LAC = \dot{m} / A \tag{6}$$

As in Eq. (5), A is the local surface area, \dot{m} is the mass of sand particles impinging on the local area per unit time, and the unit of LAC is $[\text{g}/(\text{mm}^2 \text{ hr})]$ which gives the accumulated mass of sand particles per mm^2 per hour at the sand injection rate, 0.148 g/s .

The distributions of sand particle local accretion rates at the pressure and suction sides of the test blade are displayed in Figs. 17-18 after one hour of exposure to the sand impingement, where the rotor bottom wall is outlined by black lines. The maximum accretion rate reaches $\sim 9.0 \text{ g}/(\text{mm}^2 \text{ hr})$, and the average value over the test blade is $0.46 \text{ (g}/\text{mm}^2 \text{ hr)}$. The total mass of particle impacting on the test blade in one hour is 0.318 kg , and the total sand delivered in one hour to the 22.5° rotor sector is 0.531 kg . That is, more than half of the sand particles delivered strike the test blade.

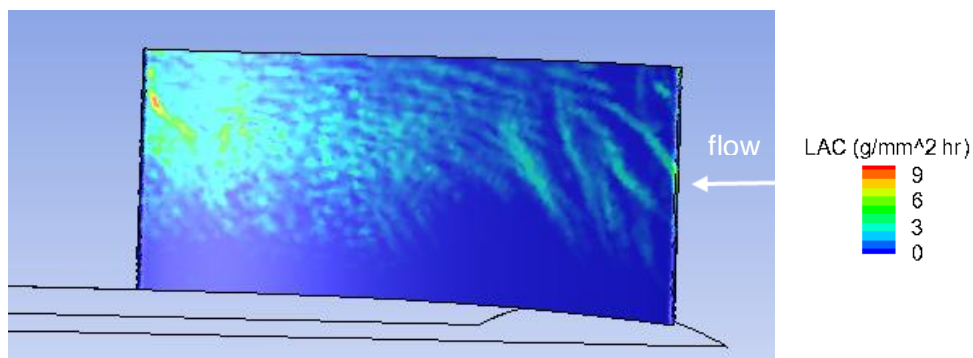


Fig. 17 Sand accretion rate distribution on the pressure side

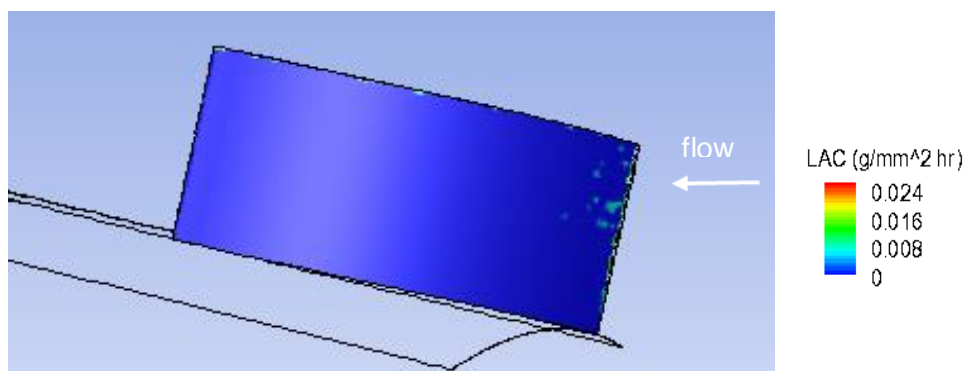


Fig. 18 Sand accretion rate distribution on the suction side

Three important features are observed in Figs. 17-18, and it should be noted that the scales in the two figures differ by orders of magnitude. First, most of the sand particles impinge on the pressure side and only a limited number of particles impact on the suction side near the leading edge. This is consistent with the observations by many researchers such as Balan & Tabakoff [2], Sugano et al [3] and Hamed et al [5]. Second, as shown in Fig. 17, severe erosion occurs mainly at the outer ~50% of the span, which agrees with the finding from Richardson et al [4]. It is also consistent with the particle trajectories observed in Fig. 16. Third, more particles impact the downstream half of the blade on the pressure side, and this can be explained by the observation in Fig. 13. Due to the inertia, particles impact the blade surface because they cannot follow exactly the airflow path-lines.

The above observations are consistent with those in the RMC compressor rig testing, although some photos in the report [9] are not sufficiently clear for comparison. Figure 19 shows the rear pressure surface of the test blade before and after 5 hours of erosion. The rear portion of the pressure side is heavily polished by particles, particularly for the upper portion. This is consistent with the simulation results in Fig. 17.

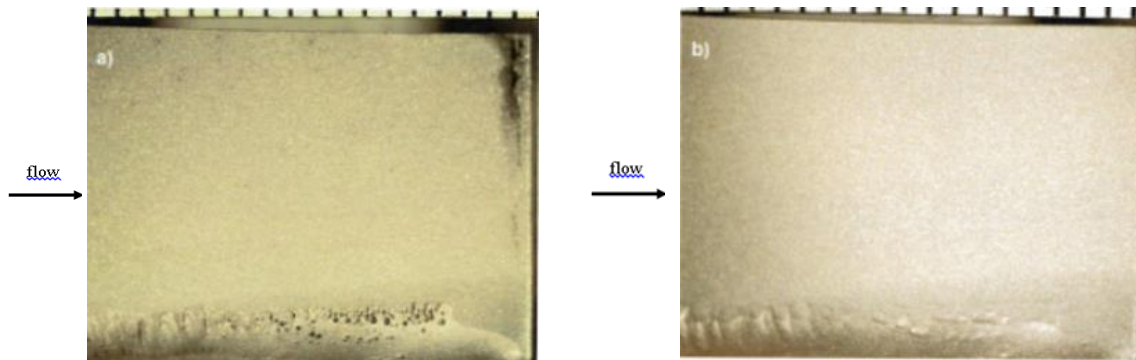


Fig. 19 Test blade rear pressure surface: (a) before erosion, (b) after 5 hours of erosion (scale in 1 mm per increment and 8x magnification)

The blade cross-section profiles before and after 5 hours of erosion are illustrated in Fig. 20. It is apparent that the blade trailing edge is sharpened due to erosion. This is also consistent with the observation in Fig. 17, where more particles impacted the trailing edge region. The comparisons between the experimental observations in Figs. 19-20 and the numerical results in Fig. 17 indicate that the developed sand erosion model is adequate for engine components made of 17-4PH steel.

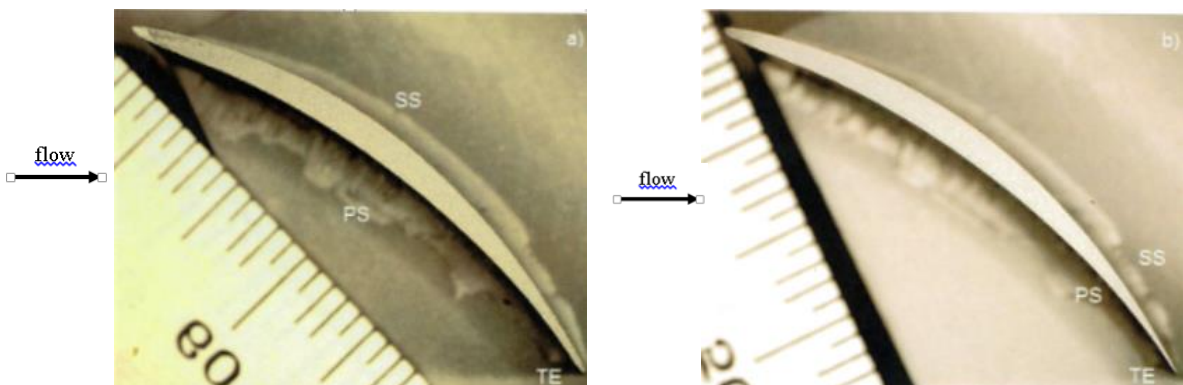


Fig. 20 Sharpened trailing edge of the test blade: (a) before erosion, (b) after 5 hours of erosion (scale in 1 mm per increment and 6.3x magnification)

In addition to the accretion rate, other parameters related to particle erosion are obtained in the simulation, which provides additional information to aid in understanding of the erosion phenomena. The velocity magnitude distributions of sand particles impacting on the pressure and suction sides are presented in Figs. 21 and 22 respectively, where the blue region means no particle impingement and the white arrow indicates the incoming flow direction. The maximum velocity magnitude reaches ~190 m/s, and the maximum value at the suction side is higher than that at the pressure side due to flow acceleration at the suction side. The distribution features are the same as Figs. 17-18, i.e., most of particles strike on the pressure side. Moreover, on the pressure side, the particle velocities are higher in the upstream region than those at the downstream portion. It is anticipated that the flow velocity near the pressure side gradually decreases as shown in Fig. 10.

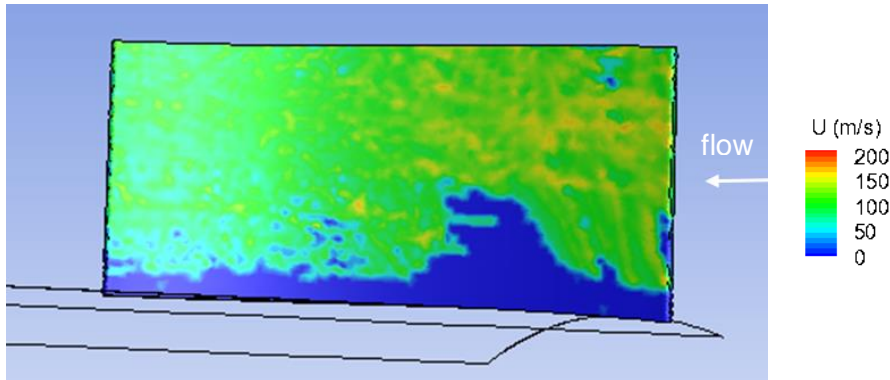


Fig. 21 Velocity magnitudes of particles impacting the blade pressure side

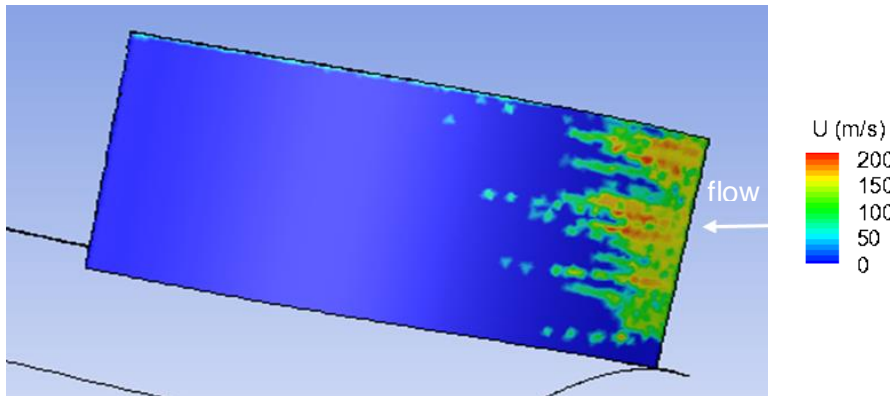


Fig. 22 Velocity magnitudes of particles impacting the blade suction side

The diameter distributions of particles impacting the blade pressure and suction sides are displayed in Figs. 23-24 respectively. The particle maximum diameter is 125 μm as defined in the air/sand inlet, and the contour features are similar to the velocity contours in Figs. 21-22. It is interesting to see that large particles more commonly strike the blade lower surfaces, instead of a uniform distribution. This can be readily explained by the variation of particle trajectories with their sizes, as shown in Figs. 15-16. The particle trajectories are determined by the cone configuration, rotor section walls and particle properties.

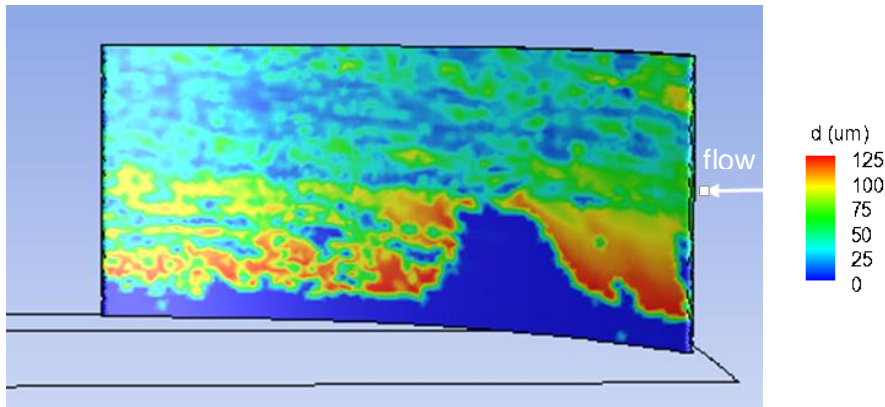


Fig. 23 Particle diameters impacting the blade pressure side

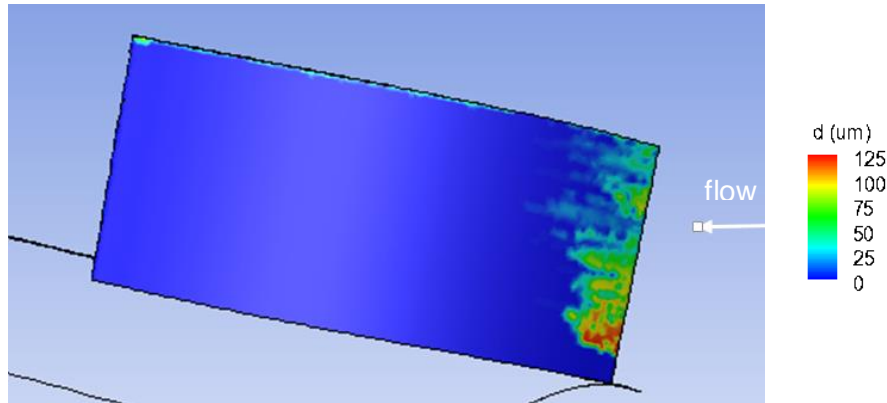


Fig. 24 Particle diameters impacting the blade suction side

The contours of sand particle accretion rate, impinging velocity and diameter in the vicinity of the leading edge are given in Fig. 25. Sand particles heavily strike the leading edge from $\sim 1/3$ of the span to the tip, and large particles hit the lower portion of the leading edge as seen in Figs. 23-24. Figure 26 is a photo of the blade cross-section profile after 5 hours testing. The round leading edge tip at the pressure side becomes bowed and blunt, which is consistent with the simulation result. Rapid erosion at the leading edge from the middle span to the tip is also observed in a similar erosion testing with the same test rig [25].

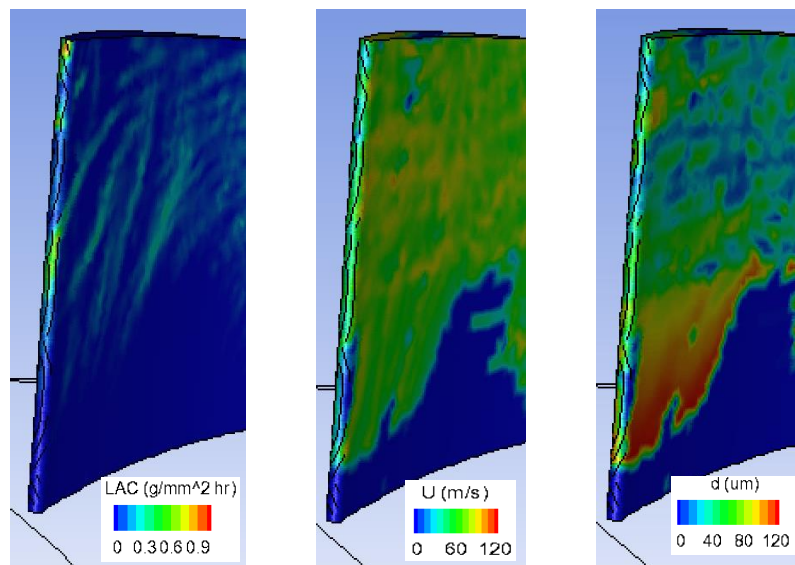


Fig. 25 Contours of sand particle accretion rate, impinging velocity and diameter near the leading edge

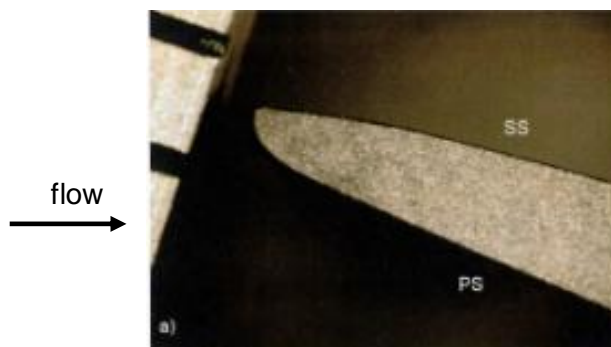


Fig. 26 Blade leading cross-section profile after 5 hours of testing (scale in 1 mm per increment and 40x magnification)

In summary, Figs. 17–26 demonstrate that the numerical simulation results are consistent with the test results from the RMC compressor rig and the experimental findings from other researchers. The sand erosion blunts the leading edge, sharpens the trailing edge, and increases pressure surface roughness. For the present rig geometry, in particular the cone geometry, few particles strike the blade root area, and more particles hit the upper area of the blade pressure side. Also, more particle accretion occurs

at the rear portion of the chord than the forward region.

4.4 Sand Erosion Rate

In the previous sub-section, the numerical results were qualitatively compared with the experimental results from the RMC and other researchers. In this sub-section, the sand erosion rate from the simulation is compared with those from other erosion models. Figures 27 and 28 display the contours of local sand erosion rate at the blade pressure and suction sides from the current simulations. As expected, severe sand erosion occurs on the pressure side, particularly at the rear upper region, and the erosion rate at the suction surface is negligible, except in the vicinity of the leading edge (note the scales differ by about two orders of magnitude). These support the features of particle accretion discussed in the previous sub-section. The maximum erosion rate reaches 6.3 ($\text{mg}/\text{mm}^2 \text{ hr}$), the average is 0.39 ($\text{mg}/\text{mm}^2 \text{ hr}$), and the blade mass loss is 0.273 (g/hr).

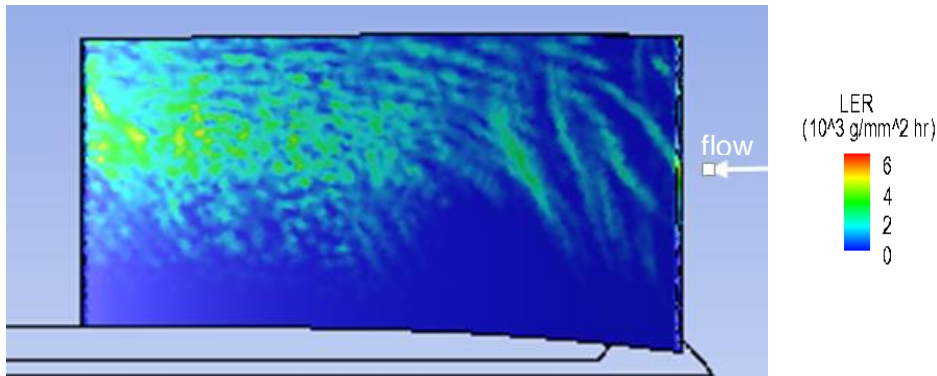


Fig. 27 Sand local erosion rate on the blade pressure side

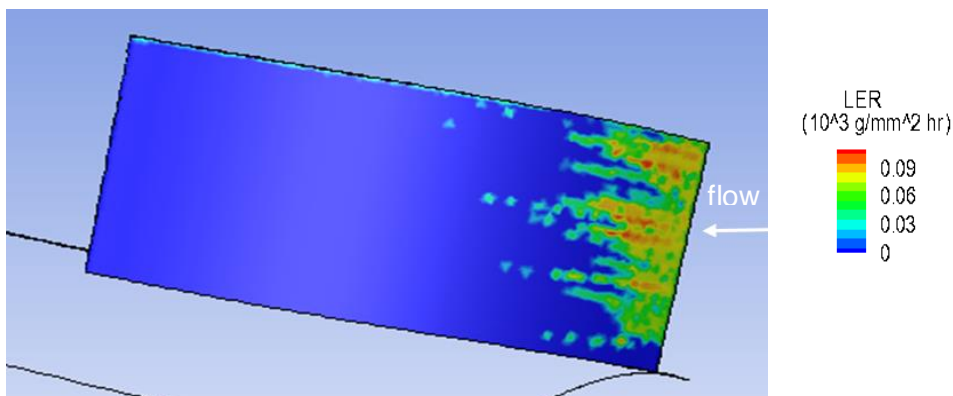


Fig. 28 Sand local erosion rate on the blade suction side

In Table 4, the predicted sand erosion rate is quantitatively compared with three other sand erosion models. The first model is Finnie Erosion model [26], and its model constants have been tuned to match the experiment data in reference [27], where 326 μm sand particles impinging on a carbon steel wall at a speed of 104 m/s. The second is McLaury model for predicting the erosion rate of sand particles on carbon steel in water [28]. The third is Oka erosion model with the constants calibrated for sand erosion on carbon steel [27]. The maximum erosion rate, average erosion rate and total blade mass loss predicted by the four sand erosion models are listed in Table 4. Recall that these numbers are obtained based on a sand flowrate of 0.148 g/s or 0.531 kg/hr passing through the 22.5° rotor sector. As shown in Table 4, the predicted values from the current model are lowest among these four models since the mechanical properties of 17-4PH steel are better than carbon steel. The predicted mass loss from the 17-4PH model is 13% lower than the average mass loss from the three carbon steel models, which reveals that 17-4PH steel has stronger resistance to sand erosion than carbon steel.

Table 4 Sand local erosion rate and blade mass loss

| model | maximum erosion rate ($10^3 \text{ g}/\text{mm}^2 \text{ hr}$) | average erosion rate ($10^3 \text{ g}/\text{mm}^2 \text{ hr}$) | total blade mass loss (g/hr) |
|---------|---|---|---------------------------------|
| Current | 6.34 | 0.393 | 0.273 |
| Finnie | 5.46 | 0.398 | 0.277 |
| McLaury | 9.76 | 0.514 | 0.357 |

| | | | |
|-----|------|-------|-------|
| Oka | 8.57 | 0.438 | 0.304 |
|-----|------|-------|-------|

5. Conclusion

Sand or other particles can cause significant degradation to propulsion system performance, and increase the cost of ownership, particularly for helicopters. Based on erosion tests on 17-4PH steel coupons, a sand erosion model has been developed. In this work, the developed erosion model has been validated against the results of the RMC compressor rig tests and other published results. A high-fidelity CFD model of the RMC test rig has been built; the two-phase, turbulent, compressible flow-field in multiple reference frames has been solved, and the developed erosion model has been implemented into the ANSYS CFD Premium software and checked step by step.

The simulation results are consistent with the test results from the RMC compressor rig and experimental findings from other researchers. Sand erosion blunts the leading edge, sharpens the trailing edge, and increases pressure surface roughness. For the present rig geometry, particularly for the cone geometry, few sand particles strike the vicinity of the blade root, and most particles hit the large upper area on the blade pressure side. More particle accretion is found at the rear half of the chord than the forward region.

The comparisons between the experimental observations and numerical results as well as a quantitative comparison with three other sand erosion models indicate that the developed sand erosion model is adequate for erosion prediction of engine components made of 17-4PH steel. The predicted mass loss from the 17-4PH model is 13% lower than the averaged mass loss from the three carbon steel models, which indicates that 17-4PH steel has stronger resistance to sand erosion than carbon steel. Furthermore, the established methodologies can also be used to evaluate the effect of erosion-resistant coating and the erosion degradation of components under actual engine operating conditions.

Acknowledgements

The authors are grateful to the Department of National Defense and the National Research Council of Canada for funding and supporting this collaborative research project. Also, many thanks go to Dr. Steve Zan for the valuable comments and suggestions in the preparation of the manuscript.

References

- [1] Grant, G. and Tabakoff, W., Erosion prediction in turbomachinery resulting from environmental particles, *Journal of Aircraft*, Vol. 12, No. 5, pp. 471–478, 1975.
- [2] Balan, C. and Tabakoff, W., Axial compressor performance deterioration, *AIAA Paper* 84-1208, 1984.
- [3] Sugano, H., Yamaguchi, N. and Taguchi, S., A study on the ash erosion of axial induced draft fans of coal-fired boilers, *TR*, Vol. 19, Mitsubishi Heavy Industries, Tokyo, Japan, Feb. 1982.
- [4] Richardson, J. H., Sallee, G. P. and Smakula, F. K., Causes of high-pressure compressor deterioration in service, *AIAA Paper* 79-1234, 1979.
- [5] Hamed, A., Tabakoff, W. and R. Wenglarz, R., Erosion and deposition in turbomachinery, *Journal of Propulsion and Power*, Vol. 22, No. 2, 2006.
- [6] Bitter, J. G. A., A study of erosion phenomena, *Wear*, 6, 1963.
- [7] Neilson, J.H. and Gilchrist, A., Erosion by a stream of solid particles, *Wear*, 11, 1968.
- [8] Wu, X. and Yang, Q., Durability & risk effects tool for adverse environmental erosion phase I, *LTR-SMM-2020-0050*, 2020.
- [9] Leithead, S., A durability test rig and methodology for erosion-resistant blade coatings in turbomachinery, M.S. thesis, *Royal Military College of Canada*, Kingston, ON, Canada, 2013.
- [10] Massouh, R., Test rig for durability testing of gas turbine blade erosion coatings, *Royal Military College of Canada*, Master of Engineering (Mechanical Engineering) Project Report, 2012.
- [11] Robinson, R.G. and Delano, J.B., An investigation of the drag of windshields in the 8-foot high-speed wind tunnel, *National Advisory Committee for Aeronautics*, Special Report Number 114, pp. 6, 1939.
- [12] Cowherd, C., Sandblaster 2 support of see-through technologies for particulate brownout, *Midwest Research Institute*, 110565.1.005, Kansas City, MO USA, 2007.
- [13] Barton, Technical data and physical characteristics for alluvial garnet abrasives. http://www.barton.com/documents/Tech%20Data%20Alluvial%20Garnet_Barton.pdf, 2012.
- [14] Ferziger, J.H. and Peric, M., *Computational Methods for Fluid Dynamics*. Springer-Verlag, New York, 2000.
- [15] ANSYS Canada Ltd., Fluent 19 documentation, 283 Northfield Drive E, Unit 21 Waterloo, ON, N2J 4G8, 2018.

- [16] Tallman, J.A., Haldeman, C.W., Dunn, M.G., Tolpadi, A.K. and Bergholz, R.F., Heat transfer measurements and predictions for a modern, high-pressure, transonic turbine, including end-walls, *Transactions of the ASME, Journal of Turbomachinery*, Vol. 131 / 021001-1, 2009.
- [17] Stiesch, G., *Modeling engine spray and combustion processes*. Springer, New York, 2003.
- [18] Morsi, S.A. and Alexander, A.J., An investigation of particle trajectories in two-phase flow systems, *Journal of Fluid Mechanics*, Vol. 55, No. 2, pp. 193-208, 1972.
- [19] Haider, A. and Levenspiel, O., Drag coefficient and terminal velocity of spherical and non-spherical particles, *Powder Technology*, Vol. 58, pp. 63-70, 1989.
- [20] Taslim, M.E., Khanicheh, A., and Spring, S., A numerical study of sand separation applicable to engine inlet particle separator systems, *Journal of the American Helicopter Society*, 54, pp. 042001-1-10, 2009.
- [21] Duffy, R.J. et al., Integral engine inlet particle separator, *Design Guide*, Vol. II, USAAMRDL-TR-75-31B, 1975.
- [22] Wakeman, T. and Tabakoff, W., Measured particle rebound characteristics useful for erosion prediction, paper 82-GT-170, *ASME Gas Turbine Conference*, London. 1982.
- [23] Taslim, M.E. and Spring, S., A numerical study of sand particle distribution, density, and shape effects on the scavenge efficiency of engine inlet particle separator systems, *Journal of the American Helicopter Society*, 55, pp. 022006-1-9, 2010.
- [24] Menter, F.R., Two-equation eddy-viscosity turbulence models for engineering applications, *AIAA Journal*, Vol. 32, No. 8, pp. 1598-1605, 1994.
- [25] Leithead, S.G., Allan, W.D.E., Zhao, L. and Yang, Q., Enhanced experimental testing of new erosion-resistant compressor blade coatings, *Journal of Engineering for Gas Turbines and Power*, Vol. 138, 112603, 2016.
- [26] Finnie, I., Some reflections on the past and future of erosion, *Wear* 186-187, pp. 1-10, 1995.
- [27] Oka, Y.T. and Yoshida, T., Practical estimation of erosion damage caused by solid particle impact, part 2: mechanical properties of materials directly associated with erosion damage, *Wear*, pp.102-109, 2005.
- [28] McLaury, B.S. et al., Modeling erosion in chokes, *Proceeding of ASME Fluids Eng. Summer Meeting*. San Diego, California. 1996.

Copyright Statement

The authors confirm that they, and/or their company or organization, hold copyright on all of the original material included in this paper. The authors also confirm that they have obtained permission, from the copyright holder of any third party material included in this paper, to publish it as part of their paper. The authors confirm that they give permission, or have obtained permission from the copyright holder of this paper, for the publication and distribution of this paper as part of the ICAS proceedings or as individual off-prints from the proceedings.